Full and ideal mixing behavior between Zr–Wd ($K_2ZrSi_3O_9$) and Ti–Wd ($K_2TiSi_3O_9$): evidences from mineral chemistry, X-ray diffraction pattern and Raman spectrum

Linlin Chang, Xi Liu, Chunming Wu, Xiaoyang Liu & Guowu Li

Physics and Chemistry of Minerals

ISSN 0342-1791
Volume 42
Number 3

Phys Chem Minerals (2015) 42:223-234
DOI 10.1007/s00269-014-0713-x

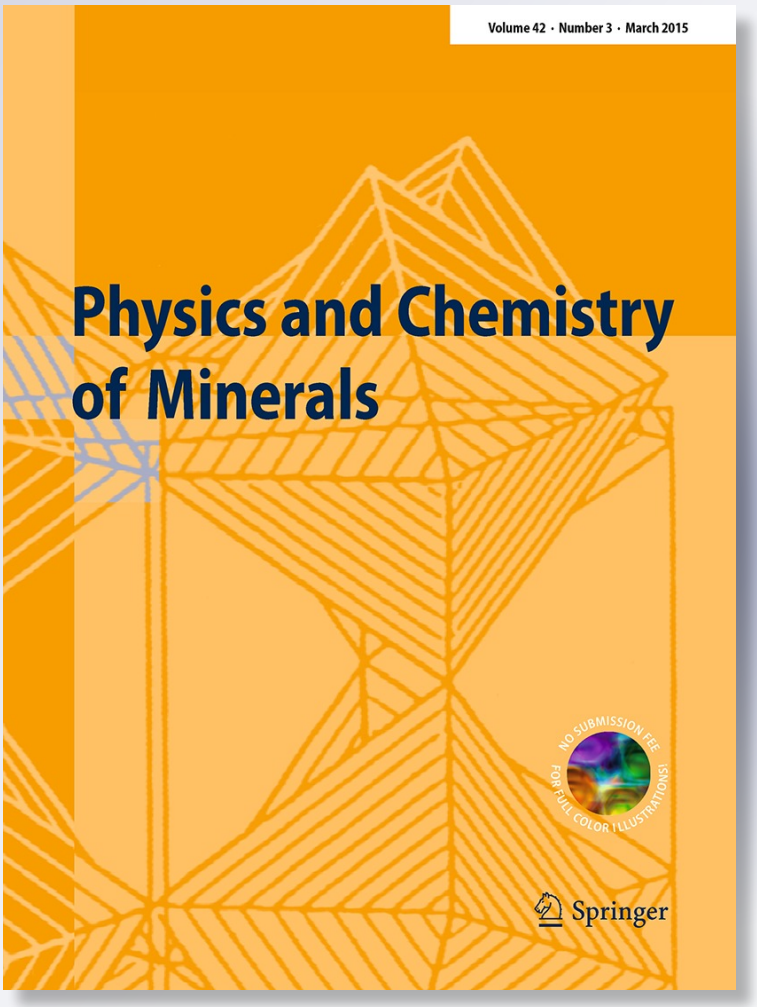

Springer

Phys Chem Minerals (2015) 42:223–234
DOI 10.1007/s00269-014-0713-x

ORIGINAL PAPER

Full and ideal mixing behavior between Zr–Wd ($K_2ZrSi_3O_9$) and Ti–Wd ($K_2TiSi_3O_9$): evidences from mineral chemistry, X-ray diffraction pattern and Raman spectrum

Linlin Chang · Xi Liu · Chunming Wu · Xiaoyang Liu · Guowu Li

Received: 15 August 2014 / Accepted: 26 September 2014 / Published online: 8 October 2014

Abstract A series of wadeite solid solutions (Wd_{ss}) along the join $K_2ZrSi_3O_9$ (Zr–wadeite, Zr–Wd)–$K_2TiSi_3O_9$ (Ti–wadeite, Ti–Wd) was synthesized at 2 GPa and 1,200–1,400 °C for 24 h with a piston-cylinder apparatus. The chemical composition data demonstrated that Ti and Zr readily substitute for each other, and a full series of Wd_{ss} exists between the Zr–Wd and Ti–Wd end-members at the *P*–*T* conditions of our synthesizing experiments. The volume–composition relationship at ambient *P*–*T* conditions did not show any significant deviation from the Vegard's law, indicating a nearly ideal mixing between the Zr–Wd and Ti–Wd. All the Raman peaks observed at ambient *P*–*T* conditions were linearly correlated with the composition, suggesting an almost full structural relaxation for the Wd_{ss}. These findings suggest that the complete mixing behavior along the join $K_2ZrSi_3O_9$–$K_2TiSi_3O_9$, as demonstrated by our high-*P* experiments, may extend to a much wider range of *P*–*T* conditions. Consequently, the coexistence of the Zr–Wd and Ti–Wd in the lamproites from the Leucite Hills, Wyoming, may be due to a chemical composition change of the magma rather than a crystal structural limit.

Keywords Crystal structural relaxation · High-*P* synthesis · Ideal mixing · Lamproite · Wadeite solid solution

L. Chang · X. Liu (✉)
Key Laboratory of Orogenic Belts and Crustal Evolution, Ministry of Education of China (MOE), Peking University, Beijing 100871, China
e-mail: xi.liu@pku.edu.cn

L. Chang · X. Liu
School of Earth and Space Sciences, Peking University, Beijing 100871, China

L. Chang · C. Wu
College of Earth Science, University of Chinese Academy of Sciences, Beijing 100049, China

X. Liu
State Key Laboratory of Inorganic Synthesis and Preparative Chemistry, College of Chemistry, Jilin University, Changchun 130012, China

G. Li
Crystal Structure Laboratory and National Laboratory of Mineral Materials, China University of Geosciences (Beijing), Beijing 100083, China

Introduction

The potassium zirconium silicate $K_2ZrSi_3O_9$ was first found in a suite of leucite lamproites from the West Kimberley area of Australia and subsequently named as wadeite by Prider (1939; Zr–Wd hereafter). Later, it was reported in the lamproites from Leucite Hills, Wyoming (Carmichael 1967; Mitchell and Steele 1992), and from Francis, Utah (Henage 1972), and in other potassium-rich rocks from both South Africa and Russia (Mitchell 1995a; Mitchell and Vladykin 1996). Its crystallographic features were investigated by Henshaw (1955; space group $P6_3/m$), and its chemical composition was documented by Carmichael (1967). According to some experimental studies done by Prider (1939), Abraham et al. (1971), Arima and Edgar (1980), Orlando et al. (2000), and Xu et al. (2005), it is thermodynamically stable at least up to 3 GPa. In contrast, the potassium titanium silicate $K_2TiSi_3O_9$ (Ti–Wd hereafter) was only discovered in the groundmass of the Middle Table Mountain madupitic lamproite from Leucite Hills, Wyoming (Mitchell and Steele 1992). Crystallographically, it shares the same space group with the Zr–Wd (Choisnet et al. 1971; Shumyatskaya et al. 1973). The experimental

study conducted by Gulliver et al. (1998) suggested that the Ti-Wd is stable at least up to 3 GPa as well.

The poikilitic coexisting of the Zr–Wd (atomic Zr/(Ti + Zr) = 0.90–0.96) and Ti–Wd (Zr/(Ti + Zr) < 0.05), observed in the Middle Table Mountain madupitic lamproite (Mitchell and Steele 1992), potentially suggests a limited solid solution behavior along the $K_2ZrSi_3O_9$–$K_2TiSi_3O_9$ join at some pressure and temperature. However, this phenomenon is compatible neither with the direct experimental observations nor with the characteristics of the crystal structures. At 0.15 GPa and 400 °C, Abraham et al. (1971) successfully synthesized an intermediate member of the isomorphic solid solution series from the Zr–Wd to Ti–Wd (Wd_{ss} hereafter). Orlando et al. (2000) further demonstrated the formation of a complete solid solution series from the Zr–Wd to Ti–Wd in a large range of *P*–*T* conditions (0.15–3 GPa and 770–1,300 °C).

The crystal structure of the Wd_{ss}, with its chemical formula as $A_2BSi_3O_9$ (A = K and B = Ti and/or Zr), is special. In the hexagonal crystal structure, the parallel layers of the three-membered rings (Si_3O_9) composed of SiO_4 tetrahedra (via corner-sharing O1) arrange in an ABAB…stacking sequence along the [001] direction, the isolated and octahedrally coordinated B atoms serve as bridges to link the rings (via corner-sharing O2), and the A atoms occupy the nine-coordinated cage sites between the layers of the rings (Choisnet et al. 1971; Shumyatskaya et al. 1973; Sakai et al. 2000; Xu et al. 2005). Consequently, this crystal structure is quite flexible, and small lattice strain caused by any physical (*P*–*T* condition) or chemical (cation substitution) change can be efficiently accommodated by slight adjustment of the structure units, without violating the basic symmetry of the Wd_{ss} (Xu et al. 2005). This flexibility, as illustrated by the extensive cation substitution taking place both on the A-sites (A = K, Rb, Cs) and on the B-sites (B = Si, Ge, Ti, Sn, Zr) (Choisnet et al. 1971; Kinomura et al. 1975; Xu et al. 2005), and by the relatively small isothermal bulk modulus and large isobaric thermal expansivity of the $K_2SiSi_3O_9$ phase (Chang et al. 2013a; Si–Wd hereafter), which has the space group of $P6_3/m$ as well (Swanson and Prewitt 1983), strongly argues for a complete solid solution series along the $K_2ZrSi_3O_9$–$K_2TiSi_3O_9$ join.

Since all the crystal structural data reported so far have been limited to the end-members Zr–Wd and Ti–Wd, it is presently unclear whether the intermediate structures are somewhat strained and energetically unfavorable compared to the end-members (Xu et al. 2005). In this study, we attempted synthesizing the solid solutions along the $K_2ZrSi_3O_9$–$K_2TiSi_3O_9$ join at 2 GPa by using a piston-cylinder apparatus. We have investigated them for their mineral chemistry characteristics by using electron microprobe, for their volume–composition relationship by using powder XRD, and for their microcrystal structural features by using Raman spectroscopy technique.

Experiment

The starting materials used in our high-*P* experiments were prepared as following. Two mixtures, aimed at the compositions of the Zr–Wd ($K_2ZrSi_3O_9$) and Ti–Wd ($K_2TiSi_3O_9$) but with corresponding extra amounts of CO_2, were first made by mixing and homogenizing under acetone reagent grade chemicals K_2CO_3, ZrO_2/TiO_2, and SiO_2 in a molar ratio 1:1:3. Following the experimental steps used by Orlando et al. (2000), these two mixtures were next pressed into pellets with a stainless steel die, then heated to remove CO_2 in Pt crucibles at 950 °C for 4 h by using a conventional muffle furnace, and finally synthesized at 1,000 °C in open air for a week. The most of the synthesized materials was finely crushed into powder and checked with a powder X-ray diffractometer (X'Pert Pro MPD system; Cu-*K*α1 X-ray radiation), and the rest was processed for examination with a scanning electron microscopy (SEM; FEI Quanta 650 FEG) hosted at the School of Earth and Space Sciences, Peking University. The powder XRD data indicated the predominance of the Zr–Wd or Ti–Wd in the product, while the SEM data indicated trace/minor amounts of baddeleyite (Badd; ZrO_2) and glass in the Zr–Wd sample, and trace amount of glass in the Ti-Wd sample, in good agreement with the observations made by Arima and Edgar (1980) and Orlando et al. (2000). The resulting two powders were mixed in appropriate proportions and homogenized under acetone to generate the final starting materials later used in the high-*P* experiments.

The series of Wd_{ss}, with the chemical formula of $K_2[Zr_xTi_{1-x}]Si_3O_9$ (*x* being equal to the atomic ratio of Zr/(Ti + Zr) and designed as 0.0, 0.2, 0.4, 0.5, 0.6, 0.8, and 1.0; Table 1), was synthesized at 2 GPa and 1,200–1,400 °C by using a piston-cylinder apparatus (Depths of the Earth Company Quickpress), newly installed at the High-Pressure Laboratory of Peking University (He et al. 2013). The cell arrangement (frictionless MgO–Pyrex–NaCl assembly) and high-*P* generating technique used in this study were identical to those used in Liu and Fleet (2009). The starting materials were contained in sealed Pt capsules (external diameter = 2.0, internal diameter = 1.8, and length = 2.5 mm). No special technique was employed in this study to prevent the experimental charge from water contamination. As demonstrated by Liu et al. (2006), the Pt capsule wall is quite open to hydrogen infiltration, so that a small amount of water should have been expected in our experimental charge. To the contrary, we actually took advantage of this small amount of water, which should have accelerated the diffusion process of the cations (especially Zr; Harrison and Watson 1983), and promoted the equilibrium state of our experimental products. The experimental *T* was measured and controlled with a Pt–$PtRh_{10}$ thermocouple (type *S*), with any potential *P* effect on its e.m.f.

Table 1 Experimental conditions, phases observed, and phase compositions for high-*P* experiments at 2 GPa

Exp #	PKU065	PKU064	PKU063	PKU057	PKU062	PKU060	PKU056
Targeted x[a]	0.0	0.2	0.4	0.5	0.6	0.8	1.0
T (°C)	1,200	1,200	1,200	1,300	1,300	1,300	1,400
Phases observed[b]	Wd_{ss}, Glass	Wd_{ss}, Badd, Glass	Wd_{ss}, Badd, Glass	Wd_{ss}, Badd, Glass	Wd_{ss}, Badd, glass	Wd_{ss}, Badd, Glass	Wd_{ss}, Badd, Glass
Composition of Wd_{ss} (wt%)[c]							
SiO_2	50.40 (49)[d]	50.80 (54)	50.30 (24)	48.83 (22)	48.16 (60)	47.44 (39)	46.67 (48)
TiO_2	22.98 (29)	19.81 (43)	15.79 (36)	10.13 (67)	7.08 (33)	2.51 (23)	–
ZrO_2	–	3.70 (40)	9.19 (56)	15.95 (64)	19.97 (87)	25.92 (41)	28.27 (13)
K_2O	26.62 (52)	25.70 (70)	24.72 (55)	25.08 (43)	24.79 (25)	24.13 (45)	25.06 (47)
Cations per 9 oxygens							
Si	2.98 (2)	3.02 (2)	3.04 (1)	3.04 (1)	3.05 (2)	3.06 (1)	3.07 (2)
Ti	1.02 (1)	0.89 (2)	0.72 (2)	0.47 (3)	0.34 (1)	0.12 (1)	–
Zr	–	0.11 (1)	0.27 (2)	0.48 (2)	0.62 (3)	0.82 (1)	0.91 (1)
K	2.01 (4)	1.95 (6)	1.90 (5)	1.99 (4)	2.00 (2)	1.99 (4)	2.10 (5)
Total	6.00 (3)	5.96 (5)	5.93 (3)	6.00 (3)	6.00 (3)	5.99 (3)	6.08 (4)
Observed x	0.00 (1)	0.11 (1)	0.27 (2)	0.51 (3)	0.65 (4)	0.87 (2)	1.00 (1)
Composition of glass (wt%)[e]							
SiO_2	63.69 (55)	67.19 (97)	70.74 (4)	63.92 (3)	67.33 (80)	55.35 (34)	68.11 (42)
TiO_2	15.30 (18)	13.36 (79)	9.83 (13)	14.35 (78)	8.97 (95)	3.70 (50)	0.05 (2)
ZrO_2	–	0.27 (6)	0.43 (3)	1.22 (9)	1.00 (6)	0.12 (6)	2.67 (64)
K_2O	8.05 (67)	6.90 (87)	7.11 (25)	7.92 (8)	6.96 (39)	8.00 (45)	17.13 (33)
Total	87.04 (26)	87.71 (55)	88.11 (19)	87.41 (98)	84.25 (69)	67.16 (77)	87.95 (75)
Observed x	0.00 (1)	0.01 (1)	0.03 (1)	0.05 (1)	0.07 (2)	0.01 (1)	1.00 (1)

[a] $x = Zr/(Ti + Zr)$

[b] Badd, baddelyite; glass, potentially water-rich melt in trace amount

[c] For every Wd_{ss}, 10 EMPA analyses were conducted. All analyses were normalized to 100 wt% before average, and standard deviation were calculated

[d] Number in the parentheses represents one standard deviation in the rightmost digit

[e] Usually, 2–5 EMPA analyses were conducted. Results must be viewed as semi quantitative

ignored. After heated for 24 h, the experiment charges were quickly quenched by turning off the electrical power supply to the piston-cylinder apparatus.

Parts of the synthetic products from the high-*P* synthesizing experiments were mounted in epoxy, polished with a series of diamond pastes, washed with an ultrasonic washing machine, carbon-coated, and examined with scanning electron microscopy (FEI Quanta 650 FEG) and electron microprobe analysis (EMPA; JEOL JXA-8100) at the school of Earth and Space Sciences, Peking University. The EMPA analytic conditions were as following: accelerating voltage 15 kV, beam current 10 nA, and beam size 5 μm. The instrument was calibrated using a range of mineral standards from Structure Probe, Inc. (synthetic silica, natural rutile, natural sanidine, and synthetic Badd for Si, Ti, K, and Zr, respectively). To obtain an average composition, ten analyses were performed on each sample, and the initial EMPA data were reduced by using the ZAF correction procedure (Table 1).

Parts of the synthesized products, dug out of the Pt capsules but without any grinding, were characterized at ambient *P*–*T* condition by using a single-crystal repeat-rotation diffraction method with a Bruker SMART APEX-CCD area-detector diffractometer hosted by the Crystal Structure Laboratory, China University of Geosciences (Beijing) (Li et al. 2009, 2011). Running conditions of the X-ray diffractometer were Mo–*Kα* X-ray radiation ($\lambda = 0.71073$ Å), operation voltage of 45 kV and current of 30 mA, data-collecting angle range from 4.5° to 40°, counting time of 60 s, and data-collecting GADDS software (Häming 2000). Using the PeakFit V4.12 software (SPSS Inc.), we analyzed the XRD patterns and obtained the positions of the diffraction peaks 100, 101, 102, 110, 111, 130, 201, 112, 202, 004, 121, 114, 300, 204, 302, 220, 124, 205, 130, 222, 106, 312, 304, 215, 313, 206, 402, 224, 410, 207, 323, and 142, from which the unit-cell parameters of the Wd_{ss} were refined. These data-processing techniques were well

established and verified in our previous studies (Liu et al. 2009; Chang et al. 2013a).

Raman spectra were collected on polished single crystals of the Wd_{ss} with a confocal micro-Raman system (Renishaw system RM-1000) in a backscattering geometry at ambient *P–T* condition. Raman signal was excited using the 514.5 nm wavelength of an Ar^+ ion laser operating at 20 mW. The Raman spectra were recorded with a counting time of 20 s, a data range from 200 to 1,200 cm^{-1}, 1 accumulation, a slit of 50 μm, and a 20× objective. The corresponding spectral resolution was 1 cm^{-1}. For every sample, four Raman analyses were performed on arbitrarily selected large crystals, and the results were much comparable. The Raman data were analyzed for the frequencies of the Raman bands with a Gauss–Lorentzian peak-fitting procedure by using the PeakFit V4.12 software (SPSS Inc.).

Results

Our high-*P* synthesizing experiments were carried out with broadly similar experimental techniques and *P–T* conditions to those in Orlando et al. (2000) and produced similar phase assemblages Wd_{ss} + Glass ± Badd (Table 1). As shown by the BSE images in Fig. 1, the Wd_{ss} phase appeared as large subhedral hexagonal-shaped crystals. The glass phase was present as a trace phase in all experimental products. Due to the small size of the glass pockets, extensive and accurate compositional data were not available; judging by the available data, the glass was mostly likely a water-rich fluid phase at the experimental *P–T* conditions (note the very low EMPA totals; Table 1). The Badd phase occurred as small bright grains, from which extensive and accurate EMPA analyses were not possible as well. We believe that it was generally a reaction residue left from the formation of the Wd_{ss}; ZrO_2 is a very refractory material, and the diffusion rate of Zr in silicates is usually very low (Harrison and Watson 1983).

The Wd_{ss} compositional data from this study are listed in Table 1 and compared in Fig. 2 with the relevant compositional data obtained in other studies. To disclose the cation substitution mechanism, the Wd_{ss} compositional data from some more complicated composition systems are summarized in Fig. 3. The powder XRD patterns are shown in Fig. 4, with the derived unit-cell parameters of the Wd_{ss} listed in Table 2 and graphically summarized in Fig. 5. The Raman spectra are displayed in Fig. 6, with the details and features of the vibrational modes of the Wd_{ss} listed in Table 3 and graphically shown in Figs. 7 and 8.

Mineral chemistry characteristics

The EMPA data suggested that the Wd_{ss} from our high-*P* experiments was compositionally homogeneous, with the standard deviation of its Zr/(Ti + Zr) ratio ranging from 0.01 to 0.04 (Table 1). In contrast, the Wd_{ss} from Orlando et al. (2000) was compositionally more scattered (their Figs. 2, 3). In their high-*P* experiments at 2 GPa and 1,200 or 1,300 °C, the experimental charge was first heated at 1,400 °C for 1 h to promote the diffusion of Zr and then kept at a lower temperature for 6.5–21 h before quenched. As noted by Orlando et al. (2000), this experimental procedure led to Zr-enriched cores for the large Wd_{ss} crystals, and consequently composition scattering. In this study, we ran our experiments at constant temperatures for a long duration (24 h) and obtained more homogeneous Wd_{ss}.

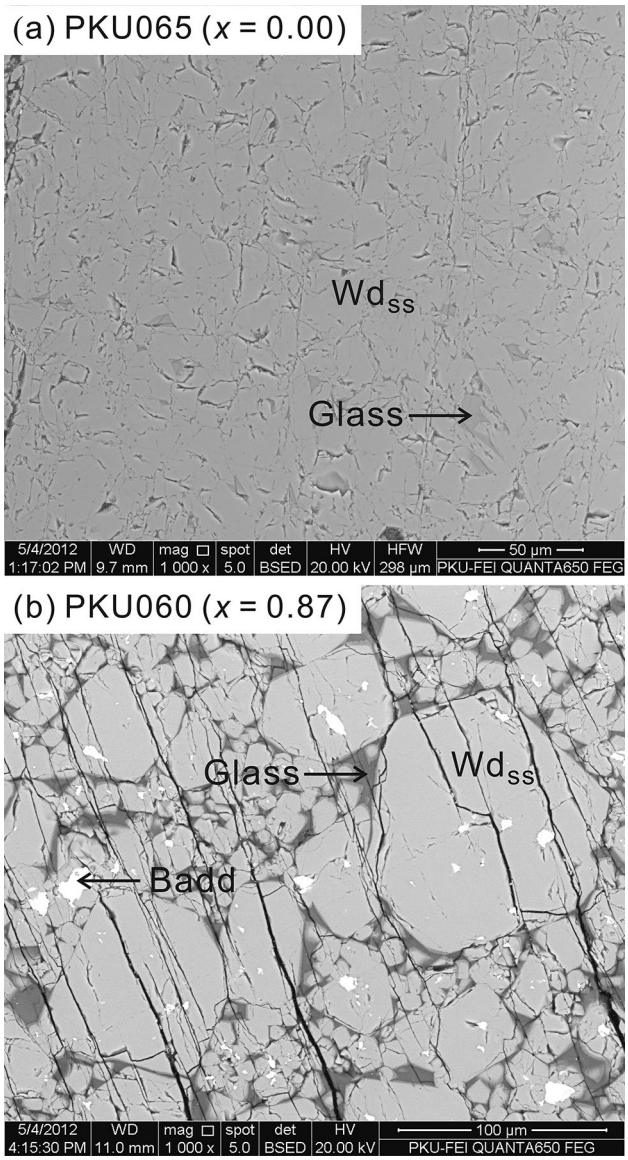

Fig. 1 Electron backscatter images showing the textures of the experimental products synthesized at 2 GPa: **a** PKU065 (1,200 °C) and **b** PKU060 (1,300 °C). Wd_{ss}, the wadeite solid solutions along the $K_2TiSi_3O_9$–$K_2ZrSi_3O_9$ join; Badd, baddelyite; glass, potentially a water-rich vapor phase

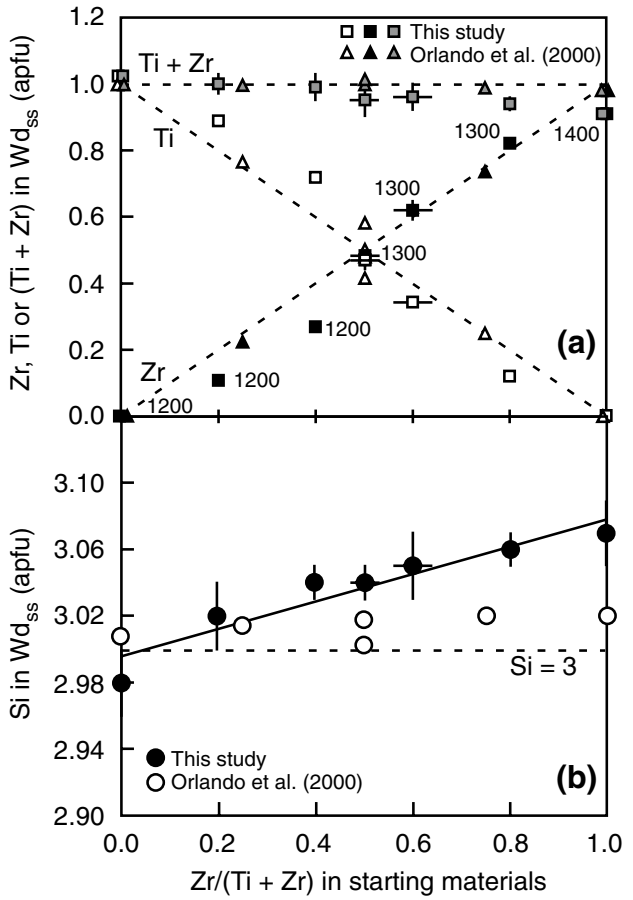

Fig. 2 Composition of Wd_{ss} along the $K_2TiSi_3O_9$–$K_2ZrSi_3O_9$ join synthesized at 2 GPa: *a* Zr, Ti or (Ti + Zr) in Wd_{ss}; *b* Si in Wd_{ss}. Numbers in *a* indicate our experimental *T*. *Empty symbols*, *filled symbols*, and *half-filled symbols* in *a* are for Ti, Zr, and (Ti + Zr) in Wd_{ss}, respectively. In most cases, the *error bars* are smaller than or equal to the sizes of the symbols. Ideally, the data points should fall on the *broken lines* in *a* and *b*. For comparison, data along the $K_2TiSi_3O_9$–$K_2ZrSi_3O_9$ join at 2 GPa from Orlando et al. (2000) were plotted as well

With respect to the targeted compositions, the presence of some residual Badd in our high-*P* experimental products implied that there must be a Zr shortage in the Wd_{ss}. Two competing factors, the Zr/(Ti + Zr) ratio in the bulk compositions and experimental temperature, clearly made their contributions. The experiments at 1,200 °C (PKU065, PKU064, and PKU063; Table 1) showed that as the Zr/(Ti + Zr) ratio in the bulk compositions increased, the Zr shortage in the Wd_{ss} became more pronounced (Fig. 2a). On the other hand, this phenomenon was much suppressed by a temperature increase, as demonstrated by the relatively small difference between the observed and designed Zr/(Ti + Zr) ratios of the Wd_{ss} at 1,300 °C (PKU057, PKU062, and PKU060; Table 1). Another potential factor was the amount of the contaminant water (or glass; Fig. 1),

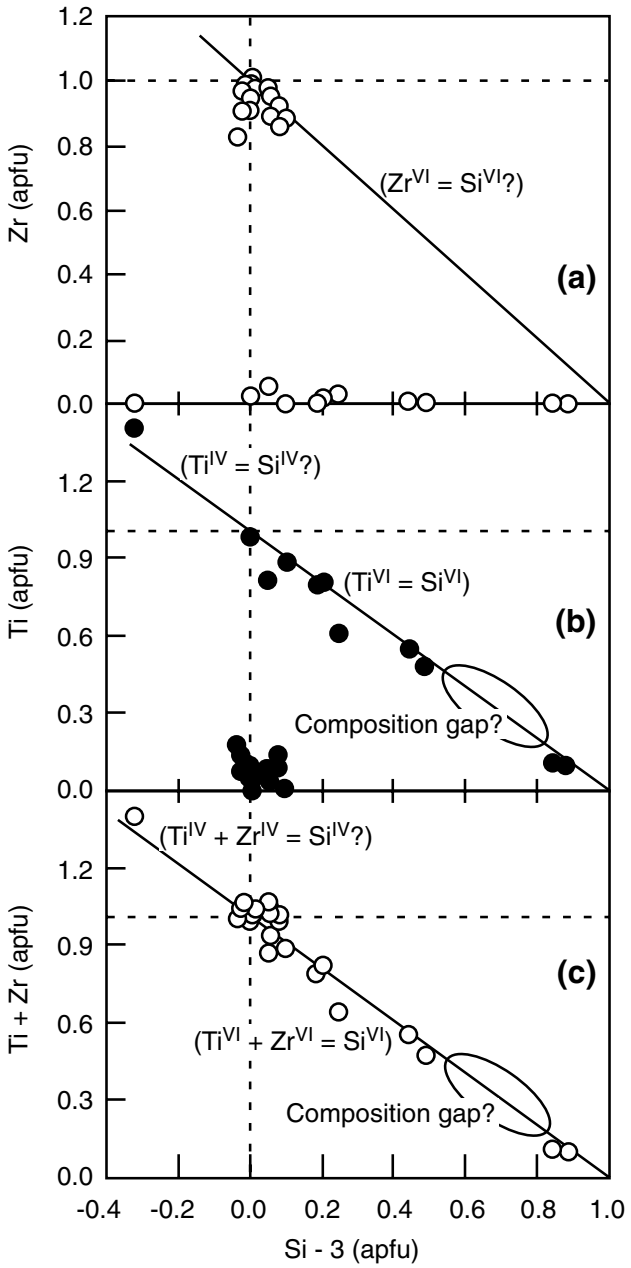

Fig. 3 Compositional data of Wd_{ss} and Si–Wd from some studies in the literature: *a* Zr versus (Si − 3); *b* Ti versus (Si − 3); *c* (Ti + Zr) versus (Si − 3). Data sources include Mitchell and Bergman (1991; 4 sets of data; West Kimberley and Leucite Hills), Cundari and Ferguson (1991; 1 set of data; West Kimberley), Mitchell and Steele (1992; 3 sets of data averaged from the EMPA data collected from the phase showing bright cathodoluminescence, the phase showing dull cathodoluminescence, and the potassium titanium silicate, respectively; Leucite Hills), Mitchell (1995b; 3 sets of data; high-*P* experiments on a sanidine phlogopite lamproite), Edger and Mitchell (1997; 7 sets of data; high-*P* experiments on an SiO_2-rich lamproite), Sakai et al. (2000; 1 set of data; a cathode ray tube), Hammond and Mitchell (2002; 7 sets of data; Swartruggens, South Africa). *Lines*, either *broken* or *solid*, are drawn to guide eye

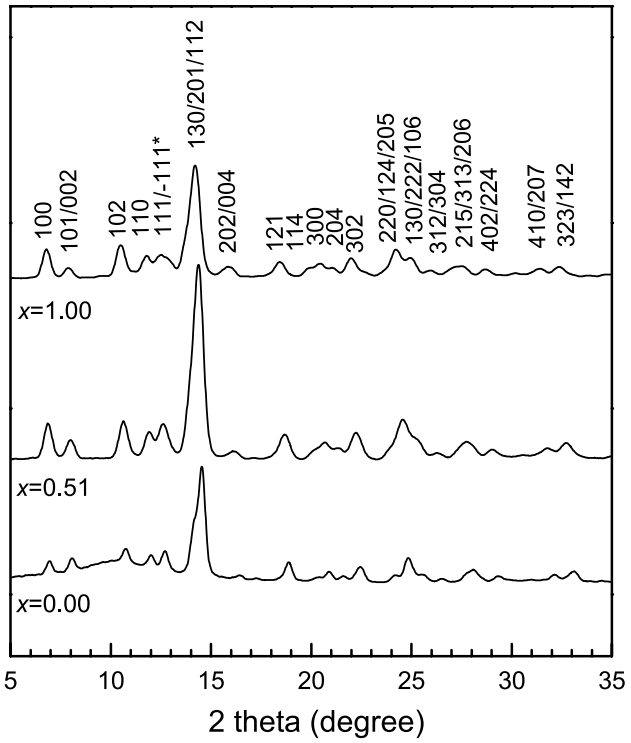

Fig. 4 Typical XRD patterns of the Wd_{ss} at ambient *P–T* condition. The Bragg peaks of Badd are denoted by *asterisk*

Table 2 Unit-cell parameters of Wd_{ss} ($K_2Zr_xTi_{1-x}Si_3O_9$) at ambient *P* and *T*

x	*a* (Å)	*c* (Å)	*V* (Å^3)	*c*/*a*
0.00 (1)[a]	6.782 (2)	9.895 (7)	394.16 (31)	1.459 (1)
0.11 (1)	6.791 (4)	9.896 (13)	395.26 (53)	1.457 (2)
0.27 (2)	6.829 (3)	9.957 (11)	402.14 (47)	1.458 (2)
0.51 (3)	6.856 (2)	10.010 (8)	407.40 (34)	1.460 (1)
0.65 (4)	6.880 (2)	10.067 (6)	412.60 (27)	1.463 (1)
0.87 (2)	6.915 (3)	10.128 (9)	419.44 (42)	1.464 (1)
1.00 (1)	6.931 (2)	10.144 (6)	421.97 (29)	1.464 (1)

[a] Number in the parentheses represents one standard deviation in the rightmost digit

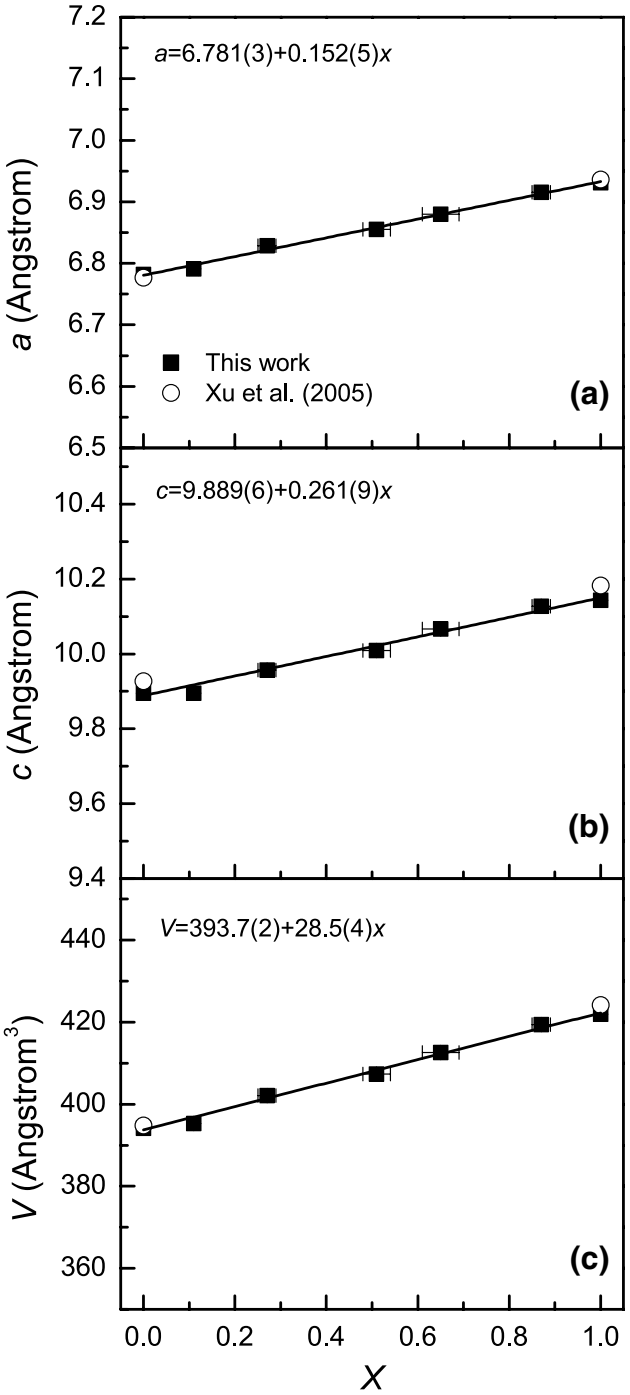

Fig. 5 Effect of composition (*x*) on the unit-cell parameters of the Wd_{ss}: *(a)* the *a*-axis; *(b)* the *c*-axis; and *(c)* the volume. The equations shown are empirically regressed from the data collected in this investigation. In most cases, the *error bars* are smaller than or equal to the sizes of the symbols

which was much dependent to the specific details of one experiment, and thus much variable.

Figure 2a indicates that for the Ti-rich bulk compositions [Zr/(Ti + Zr) < 0.5], the Zr shortage in the Wd_{ss} was largely compensated by Ti. Whatever the Zr/(Ti + Zr) ratio in these bulk compositions is, the number of the Si atoms in these bulk compositions is constant. The compensation of Zr in the Wd_{ss} by Ti, instead of by Si, therefore suggests that Ti is relatively easier to substitute Zr than Si is. This is readily understood by the difference in the ionic radii of Si^{4+} (0.4 Å), Ti^{4+} (0.605 Å), and Zr^{4+} (0.72 Å) in the BO_6 octahedra (Shannon 1976).

For the Ti-poor bulk compositions [Zr/(Ti + Zr) > 0.5], Fig. 2a indicates a Ti shortage in the Wd_{ss}, which was

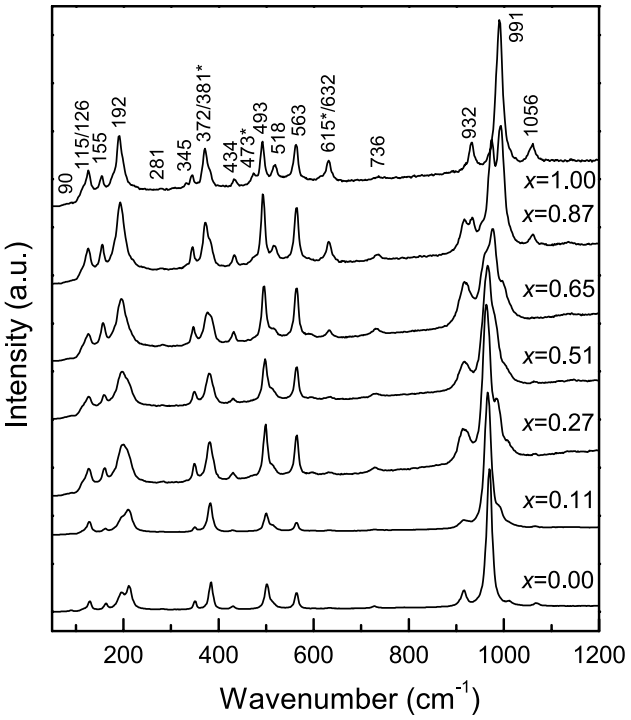

Fig. 6 Raman spectra of the Wd_{ss} at ambient *P–T* condition. The Raman peaks of Badd are denoted by *asterisk*

generally compensated by Si. It is clear that this observation is not in line with the size difference of Si^{4+}, Ti^{4+}, and Zr^{4+} in the BO_6 octahedra. Instead, this phenomenon was presumably caused by the difference in the amounts of Si and Zr available for the Wd_{ss} crystallization: The quantity and diffusion rate of Si in these bulk compositions were much larger than those of Zr.

It appears that Si may compete with Ti and Zr for the B-sites of the Wd_{ss}. Indeed, the Si cation correspondingly increased from 3 (Fig. 2b) as the total of Zr and Ti cations progressively decreased away from 1 (Fig. 2a). However, a complete solid solution series between Si–Wd and Ti–Wd or between Si–Wd and Zr–Wd probably should not be expected due to the large difference between the ionic radii of Si^{VI} (0.4 Å) and Ti^{VI} (0.605 Å), or between Si^{VI} (0.4 Å) and Zr^{VI} (0.72 Å) (Shannon 1976). Indeed, the $Si^{VI}/(Si^{VI} + Ti^{VI} + Zr^{VI})$ ratio on the B-sites of the Wd_{ss} observed in this study has been limited to ~0.07 only. In addition, Orlando et al. (2000) observed the coexisting of the Si-Wd and Wd_{ss} in one of their experiments along the $K_2ZrSi_3O_9$–$K_2TiSi_3O_9$ join (3 GPa and 1,000 °C).

The existing compositional data from some more complicated composition systems are summarized in Fig. 3. Figure 3a divides these data into two groups, one with high Zr and the other with low Zr, and shows no significant substitution between Zr^{VI} and Si^{VI}. The Zr-poor data are further divided into three subgroups (Fig. 3b): Subgroup 1 with Ti > 1, Subgroup 2 with ~0.5 < Ti < 1, and Subgroup 3 with Ti < ~0.2. The cation substitution mechanism for the data in the Subgroup 2 is generally Si^{VI} replacing Ti^{VI} in the Ti–Wd, whereas that for the data in the Subgroup 3 is most likely Ti^{VI} replacing Si^{VI} in the Si–Wd. Further, data from these two subgroups potentially suggest a composition gap between ~0.2 < Ti < 0.5 (or ~0.5 < (Si − 3) < 0.8). There is only one data in the Subgroup 1 (7 GPa/1,200 °C/6 h; Edgar and Mitchell 1997), indicating a potential cation substitution of Si^{IV} by Ti^{IV}. Figure 3c shows the correlation between the variables of (Si − 3) and (Ti + Zr) and demonstrates again the major points already discussed. We can conclude that the mixing between Zr–Wd and Si–Wd is very limited, that between Ti–Wd and Si–Wd is somewhat expanded but still incomplete, and that between Wd_{ss} and Si–Wd is probably further expanded slightly but still incomplete.

Figure 3 suggests that Ti^{IV} may partially replace Si^{IV} and enter the Si_3O_9 ring of the Wd_{ss} (Fig. 3b), but Zr^{IV} may not (Fig. 3a). This observation is generally in agreement with the differences in the cation radii of Si^{IV} (0.26 Å) and Ti^{IV} (0.42 Å), and in the cation radii of Si^{IV} (0.26 Å) and Zr^{IV} (0.59 Å) (Shannon 1976).

In summary, Fig. 2 has demonstrated that a full series of solid solutions exists between the Zr–Wd and Ti–Wd at our experimental *P–T* conditions. On the contrary, the Si–Wd may not completely mix with either the Ti–Wd or the Zr–Wd, as illustrated in Fig. 3.

Powder XRD patterns

Typical powder X-ray diffraction patterns, collected from our high-*P* synthetic products, are shown in Fig. 4. All the major peaks can be attributed to the Wd_{ss}. Due to the generally low resolution of the XRD data, however, their Rietveld analysis failed, and any fine crystal structure distortion caused by the B-site cation substitution could not be extracted. On the other hand, the XRD data were adequately accurate for the purpose of determining the unit-cell parameters.

The unit-cell parameters of the Wd_{ss} derived from these XRD patterns are given in Table 2. The unit-cell parameters of the Zr–Wd and Ti–Wd are much comparable to the values obtained by Xu et al. (2005). From the Ti–Wd to Zr–Wd, the *a*-axis increases by ~2.2(1)%, the *c*-axis by ~2.5(1)%, and the volume by ~7.1(2)%, suggesting a slightly larger effect of the B-site cation substitution on the dimension of the *c*-axis than on that of the *a*-axis, in agreement with Xu et al. (2005). Anyhow, the *c*/*a* ratio of the Wd_{ss} remains nearly constant (Table 2), implying that any perturbation to the basic unit-cell shape caused by the B-site cation substitution is largely absorbed by the flexible crystal structure of the Wd_{ss}.

Table 3 Features of Raman peaks of Wd_{ss} ($K_2Zr_xTi_{1-x}Si_3O_9$) at ambient *P* and *T*

Symmetry	$K_2SiSi_3O_9$[a]	$x = 0.00$	$x = 0.11$	$x = 0.27$	$x = 0.51$	$x = 0.65$	$x = 0.87$	$x = 1.00$	$x = 1.00$[b]	Mode assignment
E_{1g}	92	91.1 (5)[c]	91.0 (7)	90.9 (5)	90.5 (9)	90.3 (5)	89.9 (7)	89.4 (3)	91	Ring-R (*xy*) + K-T (*xy*)[d]
A_g	121	117.4 (4)	115.7 (9)	114.4 (9)	115.3 (9)	114.8 (6)	115.0 (8)	114.9 (7)	107	K-T (*z*)
E_{1g}	137	128.7 (2)	128.2 (2)	126.7 (5)	126.2 (7)	126.1 (2)	126.3 (2)	126.0 (3)	124	K-T (*xy*) + Ring-R (*xy*)
E_{2g}	177	163.3 (1)	162.4 (1)	160.0 (4)	157.1 (2)	156.0 (2)	154.5 (4)	154.8 (2)	155	Ring-T (*xy*) + K-T (*xy*)
A_g	197	195.4 (2)	196.0 (6)	193.9 (6)	193.7 (7)	195.7 (6)	193.0 (2)	192.1 (1)	194	Ring-R (*z*) + K-T (*z*)
E_{1g}	249	212.3 (1)	211.7 (3)	206.4 (4)	204.1 (7)	198.0 (5)	194.9 (3)	192.1 (1)	192	ν19 + ν1
E_{2g}	297	282.6 (2)	282.4 (2)	282.1 (2)	281.8 (2)	281.3 (2)	281.1 (2)	280.9 (2)	281	ν3 + ν14
A_g	369	350.5 (2)	350.3 (2)	350.0 (2)	347.5 (2)	347.4 (2)	345.9 (3)	345.2 (2)	345	ν3 + Ring-R (*z*)
E_{2g}	407	384.1 (1)	383.2 (6)	381.4 (1)	379.6 (1)	376.0 (2)	373.0 (1)	371.8 (2)	372	ν3 + ν14
E_{1g}	448	430.4 (3)	430.8 (3)	430.9 (6)	431.5 (3)	431.3 (4)	431.9 (4)	434.8 (2)	432	ν1 + ν19
A_g	547	501.6 (9)	500.2 (1)	499.1 (1)	495.7 (1)	494.5 (1)	494.1 (1)	492.7 (1)	493	ν3 + ν8
E_{1g}	521[e]	514.0 (8)	514.8 (9)	514.5 (8)	515.6 (6)	516.3 (3)	517.7 (2)	518.4 (4)	518	ν1 + ν19
A_g	572	564.2 (1)	564.2 (1)	564.2 (1)	563.8 (1)	563.6 (1)	563.6 (1)	563.2 (1)	564	ν9 + ν3
A_g	644	632.9 (17)	632.9 (14)	632.5 (6)	633.1 (5)	633.2 (5)	632.1 (3)	632.3 (2)	632	ν10 + ν5
E_{2g}	731[e]	728.2 (5)	728.7 (5)	728.8 (12)	731.8 (6)	733.1 (9)	734.7 (17)	735.9 (8)	736	ν16 + ν3
A_g (I)[f]		938	915.5 (1)	915.5 (1)	917.5 (3)	918.4 (2)	918.0 (2)	916.3 (3)	–	–
A_g (II)	–	–	931.9 (8)	931.5 (7)	932.0 (6)	932.2 (5)	932.8 (8)	932.4 (1)	932	ν11 + ν6
E_{1g} (I)	1,011	969.0 (1)	966.5 (1)	963.7 (1)	960.2 (2)	958.3 (1)	954.8 (5)	–	–	ν7
E_{1g} (II)/E_{2g} (I)	–	–	991.0 (2)	986.8 (2)	980.0 (1)	978.3 (1)	973.3 (1)	–	–	ν7/ν18 + ν6
E_{2g} (II)	–	–	1,010.9 (6)	1,007.2 (2)	1,001.8 (7)	999.5 (1)	993.7 (1)	990.8 (1)	992	ν18 + ν6
C[g]	–	1,068.3 (6)	1,067.4 (9)	1,064.9 (9)	1,062.1 (8)	1,061.2 (9)	1,058.5 (6)	1,056.3 (4)	1,057	

[a] Data source, Chang et al. (2013b)

[b] Data source, McKeown et al. (1996)

[c] Number in the parentheses represents one standard deviation in the rightmost digit

[d] Mode assignment is in accordance with Chang et al. (2013b). *T*, translation; R, rotation; (*xy*) after T means the translation generally occurring in the *xy* plane, whereas (*z*) after T means the translation parallel to the *z*-coordinate; (*xy*) after R means the rotating axis almost confined in the *xy* plane, whereas (*z*) after R means the rotating axis generally parallel to the *z*-coordinate. Components used to describe the vibrational modes of the C_{3h}-symmetry Si_3O_9 rings (ν1–ν19) are shown in Figs. 3 and 4 of Chang et al. (2013b)

[e] Frequency not determined by the experimental observation but by first-principles simulation (Chang et al. 2013b)

[f] Due to the two-mode behavior A_g, E_{1g} and E_{2g} appear as A_g(I) and A_g(II), E_{1g}(I) and E_{1g}(II), and E_{2g}(I) and E_{2g}(II), respectively. Note the overlapping of the E_{1g}(II) and E_{2g}(I) peaks

[g] Combination mode

The dependence of the unit-cell parameters of the Wd_{ss} on the composition is shown in Fig. 5. All the unit-cell parameters strictly follow the Vegard's law. Additionally, a good linear relation between the unit-cell parameters and the radii of the B-site cation was observed for the Ti–Wd, Zr–Wd, Si–Wd, and Ge–Wd ($K_2GeSi_3O_9$) by Kinomura et al. (1975) and Xu et al. (2005). We thus conclude that the crystal structure of the Wd_{ss} is very flexible indeed.

Raman features of the Wd_{ss}

Like Si–Wd, both Zr–Wd and Ti–Wd have the crystal structure of $P6_3/m$. According to the method of Fateley et

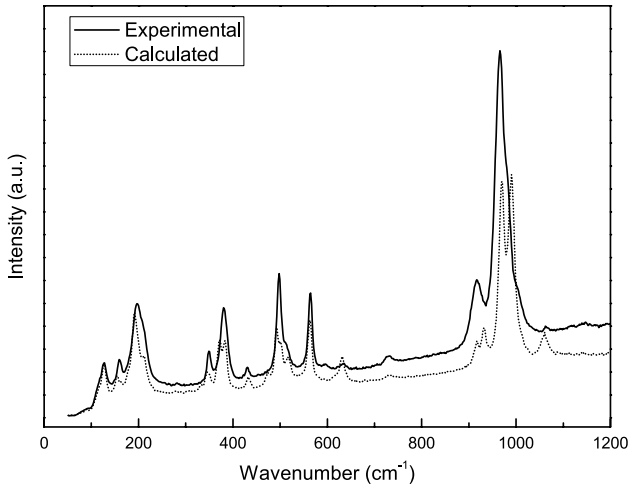

Fig. 7 Comparison between the observed Raman spectrum for the sample PKU057 ($x = 0.51$; *solid curve*) and the spectrum (*dotted curve*) obtained by combining, in equal proportions, the Raman spectra of the end-members Ti–Wd and Zr–Wd

al. (1972), the irreducible representation of the vibrational mode symmetry for the space group $P6_3/m$ is as follows (Chang et al. 2013b):

$$\Gamma = 8A_g + 6B_g + 6E_{1g} + 8E_{2g} + 6A_u + 9B_u + 8E_{1u} + 7E_{2u},$$

with A_g, B_g, A_u, and B_u being nondegenerate, and E_{1g}, E_{2g}, E_{1u}, and E_{2u} being degenerate. Among these optic modes, 22 modes ($8A_g + 6E_{1g} + 8E_{2g}$) are Raman-active, 14 modes ($6A_u + 8E_{1u}$) are infrared-active, and 22 modes are silent. Additionally, there are two acoustic modes ($1A_u + 1E_{1u}$). Assignment of the 22 Raman-active vibrational modes was done by McKeown et al. (1996; lattice dynamic calculation) and Chang et al. (2013b; first-principles simulation), and general agreement has been achieved. According to Chang et al. (2013b), the K translation accounts for three Raman modes ($1A_g$, $1E_{1g}$, and $1E_{2g}$), the external Si_3O_9 ring motion (ring rotation and ring translation) accounts for three Raman modes ($1A_g$, $1E_{1g}$, and $1E_{2g}$), and the internal

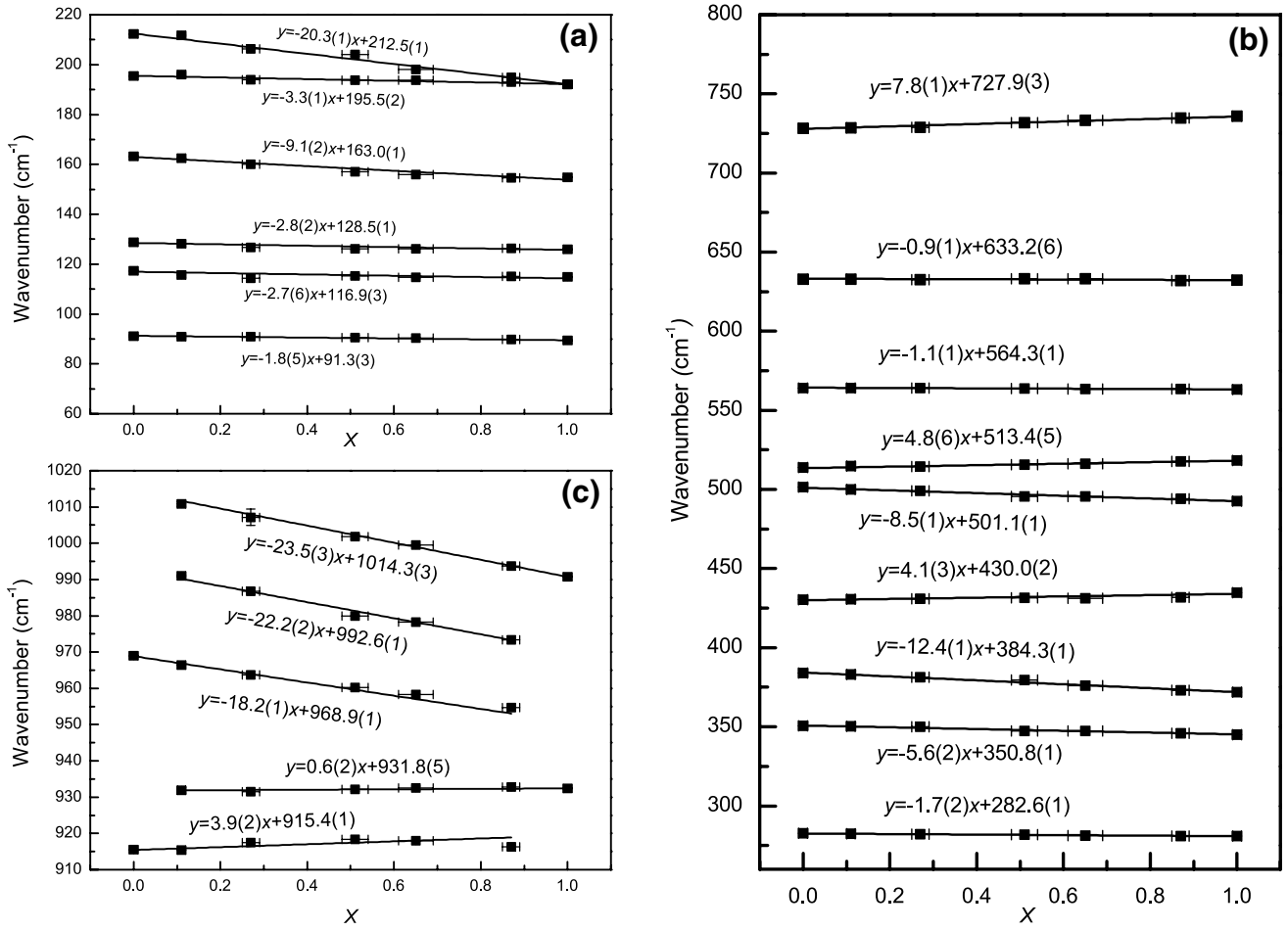

Fig. 8 Effect of composition (x) of the Wd_{ss} on the Raman peaks in the range 100–1,020 cm^{-1}: **a** 60–220 cm^{-1}; **b** 250–800 cm^{-1}; and **c** 910–1,020 cm^{-1}. The *lines* are obtained by a linear fit method. In most cases, the *error bars* are smaller than or equal to the sizes of the symbols

Si_3O_9 ring motion accounts for the rest 16 Raman modes. It should be noted that the B-site cation makes no direct contribution to any Raman mode. Taking the Si–Wd as an example, these three groups of Raman peaks are expected to appear in the wavenumber ranges of ~114–137, 92–197, and 249–1,106 cm^{-1}, respectively (Chang et al. 2013b).

The Raman spectra of the Wd_{ss} at room *P–T* condition (Fig. 6) vary systematically with the compositions of the Wd_{ss}. For the Zr–Wd ($x = 1$), only 18 Raman peaks were observed in the 50–1,200 cm^{-1} range, with 17 treated as fundamental modes and assigned according to Chang et al. (2013b), and one (~1,056 cm^{-1}) treated as a combination mode (A_g 493 cm^{-1} + A_g 563 cm^{-1}; for the details, see Table 3). Additionally, three Raman peaks were detected for the Badd phase (Keramidas and White 1974). For the Ti–Wd ($x = 0$), 18 Raman peaks were observed and assigned. For the Wd_{ss} with intermediate compositions, nearly all major Raman peaks could be similarly identified, with a few extra Raman peaks in the 800–1,200 cm^{-1} range observed and potentially explained by a two-mode behavior as proposed in the literature (Hofmeister and Chopelas 1991; Hofmeister et al. 1996).

For an exact two-mode behavior, the Raman spectrum of an intermediate member of a series of solid solutions should be identical to the superposition of the Raman spectra of its two end-members. However, attempting to pair up possible vibrational modes across a series of solid solutions always ended inconclusively due to peak broadening in the spectrum caused by cation substitution (Boffa Ballaran et al. 1999). The Raman spectra of the Ti–Wd and Zr–Wd have been combined in a 50:50 ratio and compared with the Raman spectrum collected from the sample PKU057 (Zr/(Ti + Zr) = 0.51) in Fig. 7. Remarkable similarity between these two spectra has been observed, indicating the possible role of the two-mode behavior in the Wd_{ss} solid solutions. To illustrate this point, the Raman modes A_g, E_{1g} and E_{2g} in the 800–1,200 cm^{-1} range have been fitted as two peaks [A_g(I) and A_g(II), E_{1g}(I) and E_{1g}(II), and E_{2g}(I) and E_{2g}(II), respectively], with the details listed in Table 3.

The positions of the Raman peaks of the Wd_{ss} series are shown in Fig. 8. Excellent linear correlation between the wavenumber shift and composition has been demonstrated for all the Raman lines.

As the Zr/(Ti + Zr) ratio of the Wd_{ss} increases, the two Raman peaks ascribed to the K translation ($1A_g$ and $1E_{1g}$) linearly shift to low wavenumber, suggesting a gradual increase in the K–O bonds (Fig. 8a). Indeed, the average bond length of the K–O bonds increases by ~13% from 2.983 to 3.048 Å (Xu et al. 2005).

The three Raman peaks caused by the external Si_3O_9 ring motion ($1A_g$, $1E_{1g}$, and $1E_{2g}$) also linearly shift to low wavenumber as the Zr/(Ti + Zr) ratio of the Wd_{ss} increases (Fig. 8a). This phenomenon nominally suggests that the overall change of the Si_3O_9 ring should be a gradual volume increase, which is in discrepancy with Xu et al. (2005). According to Xu et al. (2005), the Si_3O_9 ring appears to shrink both along the (001) plane and normal to the (001) plane, as hinted by the decrease in the Si–O1–Si bond angle (134.0° to 132.8°) and in the average $Si–O_1$ bond length (1.6480 to 1.6295 Å) in the former case, and by the decrease in the O2–Si–O2 bond angle (118.6° to 115.0°) and in the average Si–O2 bond length (1.602 to 1.597 Å) in the latter case. As suggested by Chang et al. (2013b), these three Raman peaks are strongly affected by the K translation motion, so that this discrepancy might abate somewhat. Anyhow, the real reason behind the conflict is currently unclear.

In contrast, the rest Raman peaks caused by the internal Si_3O_9 ring motion can linearly shift either toward low wavenumber or toward high wavenumber as the Zr/(Ti + Zr) ratio of the Wd_{ss} increases (Fig. 8b, c), suggesting a subtle and delicate structural adjustment in response to the cation substitution on the B-sites. A full description of this complicated structural adjustment is out of the scope of the present investigation.

Summarily, the almost perfect linear correlation between the peak position and the Zr/(Ti + Zr) ratio of the Wd_{ss} series obtained for all the Raman peaks suggests that the Wd_{ss} structure is quite flexible. Any local structural distortion caused by the cation substitution between Ti and Zr on the B-sites can be efficiently dissipated through out to the rest crystal structural units such as the KO_9 polyhedra and Si_3O_9 rings, leading to the formation of a full series of solid solutions along the join $K_2ZrSi_3O_9$–$K_2TiSi_3O_9$.

Discussion

Classified as a cyclosilicate, Zr–Wd actually attains a framework structure made of three-membered Si_3O_9 rings of SiO_4 tetrahedra and ZrO_6 octahedra, which are linked via corner-sharing. The K cations occupy the cavities (Henshaw 1955). In analogue to the rigid unit mode analysis proposed by Hammonds et al. (1998, and references therein), no any rigid unit modes exist in the Zr–Wd crystal structure, suggesting that no low-energy distortion involving only rotations of the Si_3O_9 rings and ZrO_6 octahedra is possible. Any deformation of the network, whatever its origin is, must contain a component of the deformation of the Si_3O_9 rings and ZrO_6 octahedra. When the substitution of the Zr cations by Ti cations on the B-sites progresses, the Si_3O_9 rings and KO_9 polyhedra gradually deform, leading to the systematic variations of the Raman peaks as shown in Figs. 6 and 8. This structural relaxation mechanism, fully in agreement with the crystallographic data disclosed by Xu et al. (2005), eventually leads to the

systematic variation of the Raman peaks with the compositional change on the B-sites of the Wd_{ss}, although the BO_6 motions actually make no contributions to the origins of the Raman peaks (Chang et al. 2013b).

Another factor important to the formation of a full solid solution series between the Zr–Wd and Ti–Wd is the relative small cation size difference between the Ti^{4+} (0.605 Å) and Zr^{4+} (0.72 Å) in the BO_6 octahedra (Shannon 1976), less than 20 %. In contrast, the Si^{4+} in a sixfold coordination is too small (0.4 Å). The relative differences between the Si^{4+} and Ti^{4+}, and between the Si^{4+} and Zr^{4+} in a sixfold coordination are by ~50 % and 80 %, respectively. Eventually, mixing gap exists along the joins $K_2SiSi_3O_9$–$K_2TiSi_3O_9$ and $K_2SiSi_3O_9$–$K_2ZrSi_3O_9$, as suggested in Fig. 3.

Our mineral chemistry data collected from our high-*P* experimental products have clearly demonstrated the complete mixing between the Zr–Wd and Ti–Wd. Our powder XRD data and Raman data have further suggested that this mixing behavior is almost ideal and consequently may extend to a much wider range of *P*–*T* conditions. The major conclusion of the current study is thus in good agreement with the earlier experimental studies (Abraham et al. 1971; Orlando et al. 2000). It follows that the poikilitic coexisting of the Zr–Wd (Zr/(Ti + Zr) = 0.90–0.96) and Ti–Wd (Zr/(Ti + Zr) < 0.05) in the lamproites from the Leucite Hills, Wyoming (Mitchell and Steele 1992), might not indicate a subsolidus unmixing process. Since the Ti–Wd phase ($K_2TiSi_3O_9$-rich) always occurred along the edges of the Zr–Wd phase ($K_2ZrSi_3O_9$-rich), as shown by Mitchell and Steele (1992), the texture relationship potentially reflected a sudden compositional change of the magma (that is, it was a signal to the chemical composition variation of the magma rather than to a crystal structural limit). Unfortunately, the supersolidus phase relationship along the join $K_2TiSi_3O_9$–$K_2ZrSi_3O_9$ has not been experimentally established so far.

Acknowledgments We are grateful for the constructive discussions on the Raman spectrum from Sean R. Shieh. We thank Guiming Shu and Bo Zhang for the technique support with the electron microprobe and scanning electron microscopy, respectively. The manuscript was significantly improved because of the constructive comments from two anonymous reviewers. We thank Dr T. Tsuchiya for processing this paper. This investigation was financially supported by the National Natural Science Foundation of China (Grant #41273072 to XL and Grant #41225007 to CW).

References

Abraham K, Flörke OW, Krumbholz K (1971) Hydrothermaldarstellung und kristalldaten von $K_2TiSi_3O_9$, $K_2TiSi_4O_{11}$, $K_2TiSi_6O_{15}$, $K_2ZrSi_3O_9$, und $K_2O.4SiO_2.H_2O$. Fortschr Mineral 49:5–7

Arima M, Edgar AD (1980) Stability of wadeite ($Zr_2K_4Si_6O_{18}$) under upper mantle conditions: petrological implications. Contrib Mineral Petrol 72:191–195

Boffa Ballaran T, Carpenter MA, Geiger CA, Koziol AM (1999) Local structural heterogeneity in garnet solid solutions. Phys Chem Mineral 26:554–569

Carmichael ISE (1967) The mineralogy and petrology of the volcanic rocks from the Leucite Hills, Wyoming. Contrib Mineral Petrol 15:24–66

Chang L, Chen Z, Liu X, Wang H (2013a) Expansivity and compressibility of wadeite-type $K_2Si_4O_9$ determined by in situ high T/P experiments, and their implication. Phys Chem Mineral 40:29–40

Chang L, Liu X, Kojitani H, Wang S (2013b) Vibrational mode analysis and heat capacity calculation of $K_2SiSi_3O_9$-wadeite. Phys Chem Mineral 40:563–574

Choisnet J, Deschanvres A, Raveau B (1971) Sur de nouvelles phases $A_2BSi_3O_9$ et $A_2BGe_3O_9$ de type wadeite ou de structure apparentee. C R Acad Sci Paris, Ser C 273:1504–1507

Cundari A, Ferguson AK (1991) Petrogenetic relationships between melilitite and lamproite. Contrib Mineral Petrol 107:343–357

Edgar AD, Mitchell RH (1997) Ultra high pressure-temperature melting experiments on an SiO_2-rich lamproite from Smoky Butte, Montana: derivation of siliceous lamproite magmas from enriched sources deep in the continental mantle. J Petrol 38:457–477

Fateley WG, Dollish FR, McDevitt NT, Bentley FF (1972) Infrared and Raman selection rules for molecular and lattice vibration: the correlation method. Wiley Interscience, New York, p 222

Gulliver CE, Edgar AD, Mitchell RH (1998) Stability and composition of K-Ti silicates, K–Ba phosphate and K–Mg fluoride at 0.85–2.6 GPa: implications for the genesis of potassic alkaline magmas. Can Mineral 36:1339–1346

Häming L (2000) GADDS like experiments using SMART CCD detectors, quick guide, application scientist, Single Crystal Diffraction. Bruker AXS GmbH, Karlsruhe

Hammond AL, Mitchell RH (2002) Accessory mineralogy of orangeite from Swartruggens, South Africa. Mineral Petrol 76:1–19

Hammonds KD, Bosenick A, Dove MT, Heine V (1998) Rigid unit modes in crystal structures with octahedrally coordinated atoms. Am Mineral 83:476–479

Harrison TM, Watson EB (1983) Kinetics of zircon dissolution and zirconium diffusion in granitic melts of variable water content. Contrib Mineral Petrol 84:66–72

He Q, Liu X, Li B, Deng L, Chen Z, Liu X, Wang H (2013) Expansivity and compressibility of strontium and barium fluorapatite: significance of the M-site cations. Phys Chem Mineral 40:349–360

Henage LF (1972) A definitive study of the origin of lamproites. MSc Thesis, Univ Oregon

Henshaw DE (1955) The structure of wadeite. Mineral Mag 30:585–595

Hofmeister AM, Chopelas A (1991) Vibrational spectroscopy of end-member silicate garnets. Phys Chem Mineral 17:503–526

Hofmeister AM, Fagan TJ, Campbell KM, Schaal RB (1996) Single-crystal IR spectroscopy of pyrope-almandine garnets with minor amounts of Mn and Ca. Am Mineral 81:418–428

Keramidas VG, White WB (1974) Raman scattering study of the crystallization and phase transformations of ZrO_2. J Am Ceram Soc 57:22–24

Kinomura N, Kume S, Koizumi M (1975) Synthesis of $K_2SiSi_3O_9$ with silicon in 4- and 6-coordination. Min Mag 40:401–404

Li G, Fang Q, Shi N, Bai W, Yang J, Xiong M, Ma Z, Rong H (2009) Zangboite, $TiFeSi_2$, a new mineral species from Luobusha, Tibet, China, and its crystal structure. Can Mineral 47:1265–1274

Li G, Xiong M, Shi N, Ma Z (2011) A new three-dimensional superstructure in Bafertisite. Acta Geol Sin 85:1028–1035

Liu X, Fleet ME (2009) Phase relations of nahcolite and trona at moderate P-T conditions. J Mineral Petrol Sci 104:25–36

Liu X, O'Neill HStC, Berry AJ (2006) Partial melting of spinel lherzolite in the system CaO–MgO–Al_2O_3–SiO_2–H_2O–CO_2–Na_2O at 1.1 GPa. J Petrol 47:409–434

Liu X, Shieh SR, Fleet ME, Zhang L (2009) Compressibility of a natural kyanite at 300 K. Prog Nat Sci 19:1281–1286

McKeown DA, Nobles AC, Bell MI (1996) Vibrational analysis of wadeite $K_2ZrSi_3O_9$ and comparisons with benitoite $BaTiSi_3O_9$. Phys Rev B 54:291–304

Mitchell RH (1995a) Kimberlites, orangeites and related rocks. Plenum Press, New York, p 410

Mitchell RH (1995b) Melting experiments on a sanidine phlogopite lamproite at 4–7 GPa and their bearing on the sources of lamproitic magmas. J Petrol 36:1455–1474

Mitchell RH, Steele I (1992) Potassian zirconium and titanium silicates and strontian cerian perovskite in lamproites from the Leucite Hills, Wyoming. Can Mineral 30:1153–1159

Mitchell RH, Vladykin NV (1996) Compositional variation of pyroxene and mica from the Little Murun ultrapotassic complex, Aldan Shield, Siberia. Mineral Mag 60:907–925

Orlando A, Thibault Y, Edgar AD (2000) Experimental study of the $K_2ZrSi_3O_9$ (wadeite)-$K_2TiSi_3O_9$ and $K_2(Zr, Ti)Si_3O_9$-phlogopite systems at 2–3 GPa. Contrib Mineral Petrol 139:136–145

Prider RT (1939) Some minerals from the leucite-rich rocks of the west Kimberley area, Western Australia. Mineral Mag 25:373–387

Sakai K, Nakagawa T, Okuno M, Kihara K (2000) A mineral wadeite in glass, occurrence and crystal structure. J Miner Petrol Sci 95:24–31

Shannon RD (1976) Revised effective ionic radii and systematic studies of interatomic distances in halides and chalcogenides. Acta Crystallogr A32:751–756

Shumyatskaya NG, Blinov VA, Voronkov AA, Ilyukhin VV, Belov NV (1973) Hydrothermal synthesis and crystal structure of Ti wadeite. Soviet Phys Dokl Crystall 18:17–19

Swanson DK, Prewitt CT (1983) The crystal structure of $K_2Si^{VI}Si^{IV}_3O_9$. Am Mineral 68:581–585

Xu H, Navrotsky A, Balmer ML (2005) Crystal-chemical and energetic systematics of wadeite-type phases $A_2BSi_3O_9$ (A = K, Cs; B = Si, Ti, Zr). Phys Chem Mineral 32:426–435